Engineered Science
DOI: https://dx.doi.org/10.30919/es1810

Enhanced Photocatalytic Carbon Dioxide Reduction to Carbon Monoxide via 2D g-C_3N_4 Modifying Homologous Perovskite $CsPbBr_3$/$CsPb_2Br_5$ Heterojunction

Shiding Zhang,[1,2] Yuhua Wang,[1,*] Yitong Wang,[1] Yao Guo,[2] Sri Hari Kumar Annamareddy[3,*] and Haijun Zhang[1]

Abstract

Developing stable and efficient photocatalysts for carbon dioxide (CO_2) reduction remains challenging due to the inherent limitations of homologous halide perovskites. While $CsPbBr_3$/$CsPb_2Br_5$ heterojunctions exhibit promising band alignment for photocatalytic reactions, their practical application is hindered by the instability of $CsPbBr_3$ quantum dots and the low activity of $CsPbBr_3$. Herein, we propose a modification strategy through the physical recombination of 2D g-C_3N_4 nanosheets with $CsPbBr_3$/$CsPb_2Br_5$ heterojunctions. The constructed type I-II heterojunction architecture establishes dual charge-transfer channels, where g-C_3N_4 serves as an electron reservoir while the perovskite heterojunction provides CO_2 activation sites. Under visible light, the optimized composite achieves a record carbon monoxide (CO) production rate of 28.17 μmol g-1 h-1, representing 4.5 and 4.6 times enhancements over pristine g-C_3N_4 and $CsPbBr_3$/$CsPb_2Br_5$, respectively. Mechanistic studies reveal that the interfacial electric field between g-C_3N_4 and perovskites prolongs carrier lifetime and reduces the energy barrier for CO desorption (ΔG = -0.54 eV). This study resolves the stability-activity trade-off in perovskite photocatalysts and provides a generalizable paradigm for designing 0D/2D hybrid systems in solar energy conversion.

Keywords: Photocatalytic CO_2 reduction; Type I-II ·homologous perovskite heterojunction; g-C_3N_4 modifying;·g-C_3N_4/$CsPbBr_3$/$CsPb_2Br_5$.

Received: 15 July 2025; Revised: 01 October 2025; Accepted: 03 October 2025.
Article type: Research article.

1. Introduction

In the field of materials science today, photocatalytic reduction of carbon dioxide has received significant attention for its potential to solve environmental and energy challenges.[1-5] The process involves converting carbon dioxide into value-added chemicals or fuels using solar energy and suitable catalysts. Therefore, the research focuses on searching for efficient, stable, and unique photocatalytic materials.[6] In particular, perovskite materials with the general equation ABX_3 (A is an organic or inorganic cation, B is a metal cation, and X is a halide anion) show excellent light absorption and charge transport characteristics, which makes it have great application potential in the field of photoelectric device photocatalysis.[7-11]

Among halide perovskites, inorganic perovskite $CsPbBr_3$ quantum dot,[12] and 2D $CsPb_2Br_5$,[13] has become the focus of photocatalytic applications because of its relatively good thermal and chemical stability.[14,15] $CsPbBr_3$ has a suitable band gap (about 2.36eV),[16] can absorb ultraviolet and visible light, and its photogenerated carrier has a long diffusion length and high mobility, which is favorable for charge transport and separation in photocatalytic reactions. However, a single $CsPbBr_3$ and $CsPb_2Br_5$ as a photocatalyst still has some disadvantages.[17,18] For example, the recombination rate of photogenerated carriers is high, resulting in limited photocatalytic efficiency. In addition, the stability of $CsPbBr_3$ under wet and light conditions still needs to be improved, which limits its practical application. To overcome the limitations of a single component, researchers have explored various theoretical and experimental methods to enhance

---

[1] *State Key Laboratory of Advanced Refractories, Wuhan University of Science and Technology, Wuhan, 430081, China*

[2] *Henan Joint International Research Laboratory of Nanocomposite Sensing Materials, Anyang Institute of Technology, Anyang, 455000, China*

[3] *Department of Chemical and Petrochemical Engineering, University of Nizwa, Nizwa, 616, Oman*

* *Email*: wangyuhua@wust.edu.cn; (Y. Wang); annamareddy@unizwa.edu.om (H. K. Annamareddy)

photocatalysis, including covalent,[19] non-covalent modifications, doping,[20,21] and others.[22,23]

Although the homologous perovskite $CsPbBr_3/CsPb_2Br_5$ can form type II heterojunction,[24-26] the photocatalytic performance has been improved to some extent, but it still faces challenges.[27] On the one hand, the stability of $CsPbBr_3$ and $CsPb_2Br_5$ itself has not been completely solved, and decomposition may occur during the photocatalytic reaction, affecting the service life of the catalyst.[25] On the other hand, the charge transport efficiency at the heterojunction interface still has room to improve, and the interface defect may lead to carrier recombination. To solve these problems, researchers have adopted a variety of solutions, such as surface passivation treatment,[28] through the introduction of organic ligands,[29] or inorganic passivation,[30] agents to reduce surface defects,[31] and improve stability, optimize the preparation process, precisely control the formation process of heterojunction, in order to improve the interface quality and charge transfer efficiency. In terms of improving stability, packaging technology can effectively isolate the external water and oxygen to prevent the decomposition of $CsPbBr_3$. At the same time, chemical modification of $CsPbB_3$, such as doping other elements or creating a vacancy,[32] can also improve its environmental adaptability to a certain extent.

$CsPbBr_3/CsPb_2Br_5$ heterojunction has shown broad application prospects in photocatalysis. Photolytic water hydrogen production,[33] can use solar energy to split water into hydrogen and oxygen,[34] providing the possibility of clean energy production. In the degradation of organic pollutants,[35] the heterojunction can effectively catalyze the degradation of various organic pollutants, such as dyes,[36] phenolic compounds,[37] and others,[38] which helps solve the problem of environmental pollution. In addition, in the field of carbon dioxide photoreduction, the $CsPbBr_3/CsPb_2Br_5$ heterojunction also has potential applications, promising to convert carbon dioxide into valuable fuels or chemicals.[25] However, due to the stability of carbon dioxide (CO_2) as a linear covalent molecule, its slow multi-electron reduction kinetics,[39] also makes it difficult to be reduced to CO.

In order to further improve the performance of the $CsPbBr_3/CsPb_2Br_5$ heterojunction, an N-type or P-type semiconductor with appropriate band structure was used to enhance the visible light absorption and maintain the stable reducing ability of the photogenic electrons in the interface,[40,41] thereby improving the overall photocatalytic efficiency of CO_2 reduction. Man Ou *et al*.[2] anchored $CsPbBr_3$ quantum dots on NH_X-rich porous $g\text{-}C_3N_4$ nanosheets to construct a composite photocatalyst for photocatalytic CO_2 reduction, showing good stability and excellent yield. It is worth noting that the use of acetonitrile and ethyl acetate as reaction media, rather than the water-saturated carbon dioxide conditions, which reflects that there are unstable factors in the system. Hierarchical band structure matching and good contact between interfaces are achieved, and multi-heterojunction studies are carried out, mainly focusing on metal oxides,[42] sulfides,[43] and semiconductor materials.

In this study, $g\text{-}C_3N_4$ modified to form a stable heterostructure is an innovative idea. $g\text{-}C_3N_4$ is a non-metallic semiconductor material with a unique two-dimensional layered structure,[44,45] good chemical stability, suitable bandgap (about 2.9 eV),[46] and excellent optical properties. The physical composite of $g\text{-}C_3N_4$ with the $CsPbBr_3/CsPb_2Br_5$ heterostructure forms a new heterostructure with many advantages.

Due to its ideal bandgap at the conduction (CB) and valence (VB) sides of -0.61 eV and 2.36 eV (vs. NHE), it has attracted much attention in water decomposition and photocatalytic CO_2 reduction reactions. In addition, $g\text{-}C_3N_4$ has the advantages of simple preparation, good photoelectrochemical properties, strong adsorption capacity, good thermal stability, and acid and alkali chemical resistance.[47] According to band matching, the conduction and valence positions of $g\text{-}C_3N_4$ were well matched to the perovskite homologous heterojunction $CsPbBr_3/CsPb_2Br_5$. This kind of matching can be regarded as a kind of modification, which is beneficial to the separation of photogenerated carriers. This matching can form a more efficient built-in electric field in the composite heterojunction, from perovskite to $g\text{-}C_3N_4$, further facilitating the separation and transport of photogenerated carriers.[4] Therefore, under light excitation, the photogenic electrons generated by the $g\text{-}C_3N_4$ Type I-II heterojunction quickly transferred to the conduction band of the $CsPbBr_3$. At the same time, the holes remained in the $g\text{-}C_3N_4$ band, significantly reducing the carrier recombination.

We designed a reasonable ternary heterojunction structure of $g\text{-}C_3N_4$/ $CsPbBr_3/CsPb_2Br_5$ with significant photocatalytic activity. In addition, density functional theory (DFT) and Gibbs free energy calculations provide a valuable reference for the results of rapid charge separation and transport processes within the heterojunction of this type I-II heterojunction. In terms of stability, the chemical stability of $g\text{-}C_3N_4$ protects the $CsPbBr_3/CsPb_2Br_5$ heterojunction. On the one hand, $g\text{-}C_3N_4$ acts as a physical barrier, reducing moisture and oxygen in the external environment to contact the $CsPbBr_3/CsPb_2Br_5$, reducing the decomposition of $CsPbBr_3$. On the other hand, the interaction between $g\text{-}C_3N_4$ and $CsPbBr_3/CsPb_2Br_5$ forms a stable type I-II heterojunction, which enhances the structural stability of the heterostructure and inhibits the formation and spread of defects at the interface.

A photocatalytic CO_2 reduction experiment was performed to verify our calculations. This type I II heterostructure superior to $g\text{-}C_3N_4$, $CsPbBr_3/CsPb_2Br_5$, and $g\text{-}C_3N_4$/ $CsPb_2Br_5$ catalyst in performance. In terms of reduction of CO_2 to CO. The highest CO yield of type I II heterostructure was 28.14 $\mu mol\ g^{-1}\ h^{-1}$, which was higher than the rate of pure $g\text{-}C_3N_4$, $CsPbBr_3/CsPb_2Br_5$ and $g\text{-}C_3N_4$ /$CsPb_2Br_5$ binary composite were about 4.5, 4.1, and 4.6 times, respectively. This work provides a very valuable guidance for the development of efficient heterojunction structures by g-C_3N_4 modification in photocatalyst applications.

2. Experimental and theory section

2.1 Chemicals and reagents preparation

Cesium carbonate ($CsCO_3$), oleic acid (OA), oleylamine (OLA), Lead(II) bromide ($PbBr_2$, 99.99%, Sigma-Aldrich), octadecylene (ODE, Alfa-Aesar) n-hexane (Alfa-Aesar), Ethyl acetate(EA) urea (Sigma-Aldrich) The water used in the whole experiment was deionized water prepared by ourselves. The high purity nitrogen (99.999%) and argon (99.99%) are sourced from commercial companies from Zhengzhou. All reagents and solvents are of analytical grade and directly used without further purification from the Scientific Compass Company.

2.2 Preparation precursor of Cs-OA

Based on reference,[4,48] we synthesized the precursor. We prepare the precursors. Firstly, 0.422g (0.125 mmol) white $CsCO_3$ power and 20 mL octadecylene (ODE) were added into a 50 mL three-necked flask with air pumped out. The whole process is protected by nitrogen gas. The mixture was heated at 120 ℃ for 30 minutes under nitrogen flow and 800r/min magnetic stirring. The water in the solvent is removed by pumping three times. Then, adjust the heating setting to quickly heat up to 150 ℃ to completely dissolve white cesium carbonate power, and then control the temperature to slow down to 120 ℃, turn off the heat button, and get the buff transparent mixture down to room temperature. We get the cesium oleate precursor. Store tightly. Waiting for use.

2.3 Preparation of g-C_3N_4

In our sample, buff carbon nitride(g-C_3N_4) nanosheets were prepared by direct thermal treatment.[44] 25 g urea is used at 530 ℃ in a muffle furnace for 2 hours at 5 ℃/min heating rate. The reaction occurred in an alumina crucible equipped with an airtight lid to prevent any evaporation of the precursor and the loss of associated gas. A fluffy pale yellow colored powder was obtained, which was termed g-C_3N_4. Then, the product was annealed from 530 ℃ to room temperature at 5 ℃/min. However, the samples are an amorphous graphite-phase nitrogen carbide, so there are no diffraction lattice fingers in Field emission transmission electron microscopy (FETEM) experiments in our monomers and composites.

2.4 Preparation of 0D/2D heterojunction $CsPbBr_3$/$CsPb_2Br_5$

Based on the literature,[24] 0D/2D heterojunction $CsPbBr_3$/$CsPb_2Br_5$ can be synthesized in situ by one-pot. First, 0.216g, 0.385g, 0.414g, 0.484g, and 0.585 g $PbBr_2$ and 20 mL ODE were added into a 50 mL three-neck flask, respectively. The temperature of the solution mixture was increased up to 120 ℃ for 30 minutes under the argon gas flow. Vacuuming removes moisture from the solvent a few times until all the $PbBr_2$ power is dissolved, and the solution appears light yellow. Then, OA (2 mL) and OAm (2 mL) were added to the mixture solution, and then the solution was heated to 190 °C until all white $PbBr_2$ dissolved completely. Subsequently, 2 mL of Cs-oleate solution was added to this solution, then vacuum, argon protection, and the reaction was terminated at 120 minutes. The reaction solution was cooled in an ice-cold water bath, collected by centrifugation at 9000 rpm for 8 min, and then washed with 25 mL of n-hexane or ethyl acetate, alternatively. The separated samples were vacuum-dried, and the other samples were redispersed in hexane to form a long-term colloidal stable solution for further use. The obtained samples will be further named as 0D2D4:0, 0D2D2:1, 0D2D1:1, 0D2D1:2, 0D2D 0:4 respectively. It should be particularly noted that when characterizing performance, we often select the 1:1 group as the representative of 0D2D homologous perovskite $CsPbBr_3$/$CsPb_2Br_5$ for comparison with other composites.

2.5 Preparation g-C_3N_4/ $CsPbBr_3$/$CsPbBr_5$ (gCN/0D/2D) composites

In this composite synthesis process,[27,49] firstly, 76.3mg 0D/2D1:1 heterojunction $CsPbBr_3$/$CsPb_2Br_5$ white powders were added into 30 mL octadecylene, the mixture was stirred 800r/min for 30min and maintained at room temperature under the protection of nitrogen. Then, 4, 8, 16 mg of the pale yellow 0D/2D $CsPbBr_3$/$CsPb_2Br_5$ was added to the solution and stirred for another 12 hours under nitrogen protection. The product was washed multiple times with n-hexane and dried at 80 °C in the vacuum oven. In the composites, the g-C_3N_4 and 0D/2D heterojunction $CsPbBr_3$/$CsPb_2Br_5$ can form a g-C_3N_4/$CsPbBr_3$/$CsPb_2Br_5$ ternary heterojunction, the obtained samples will be further named as, gCN0D2D-4, gCN0D2D-8, gCN0D2D-16, respectively.

2.6 Catalyst characterization instruments

The physical morphological structure and chemical properties of all the as-prepared samples were characterized and tested by using the following instruments.

X-ray diffraction (XRD, Cu Kα, Empyrean, Panaco, Netherlands, 2017) collects samples' structure and phase composition with a 5-90° scan range and a step size of 0.02°. The optical absorption behavior was studied using Fourier transform infrared spectroscopy (FTIR, ShimadzuIRTracer-100, Japan, 2017) and Ultraviolet-visible (UV-vis) diffuse reflectance spectra (UV-3600Plus DRS, Shimadzu, Japan, 2017).

Microstructure and morphology were analyzed by Scanning Electron Micrograph (JSM-IT800, JEOL, Japan, 2022) and Field emission transmission electron microscopy (FETEM) (Talos F200S, FEI, USA, 2017) with an energy-dispersive X-ray spectrometer (EDX). Time-resolved transient photoluminescence spectra (Edinburgh FLS980, excitation wavelength of 360 nm, England, 2017) obtained the decay curves.

X-ray Photoelectron Spectroscopy XPS (Thermo

Scientific, USA, 2018) was tested by an ultrahigh vacuum VG ESCALAB 250 electron spectrometer and passed Energy 40.0 eV with Al Kα_1 X-rays. The valence band was also measured. Photoluminescence (PL) spectra (LabRAM HR Evolution HORIBA Jobin Yvon, France, 2017) were recorded using a 325 nm laser excitation. A vacuum oven (ZDF6050 Yiheng, shanghai, 2024) was used to dry the samples at 80 °C for 8 hours.

2.7 Photoelectrochemical measurements

In the photoelectrochemical test experiment, the traditional three-electrode system is adopted, including the Pt foil counter electrode, the saturated Ag/AgCl reference electrode and the working electrode. Under the condition of the same catalyst dosage, the working electrode was obtained by the dip coating and drying method. The detailed process is as follows.

First, preparing 5 mg of the samples, dispersing it in 5 mL of n-hexane and simultaneously add 10 µL Nafion adhesive as the binder, ultrasonicate for 10 minutes to form a uniform suspension. Second, measuring 10 µL suspension, dip-coating on the Indium Tin Oxides (ITO) conductive glass, the effective exposed surface is approximately about 1×1 cm^2. Third, the prepared ITO samples were dried in a vacuum oven at 80 °C for 60 minutes. Subsequently, preparing 150 mL of tetrabutylammonium hexafluorophosphate acetonitrile solution with a concentration of 0.08 mol/L. Before the experiment, the electrolyte was purged with high-purity N_2 gas to remove the effects of water and air. The photoinduced current density versus time (i-t curve) was tested at a ±0.1 V bias potential under a solar simulator xenon light source (500 W) switching on and off mode. The electrochemical impedance spectroscopy (EIS Z'-Z'' curves) was tested within a frequency ranging from 100000 Hz to 0.01 Hz, and open circuit potential.

2.8 Photocatalytic CO_2 reduction

The photocatalytic CO_2 reduction experiment was conducted by applying the photocatalytic activity evaluation system. The model of this system is CEL-PAEM-D8, which is from Beijing Zhongjiao Jinyuan Technology Co. LTD. This system includes a gas chromatograph, an air generator, a hydrogen generator and a CO_2 circulation reactor. The top window is transparent quartz glass and is loaded with an optional light wave truncation unit. he reaction temperature within the system is kept constant at 6 ℃ through the external circulation of the cooling water system. A 500 W xenon lamp is placed 2-3 cm away from the photocatalytic reactor. The photocatalyst (10 mg) was ultrasonically dispersed in a glass Petri dishes with a diameter of 50 mm and the organic solvent was removed by vacuum drying. After uniform dispersion, the exposed area is approximately 0.02 square meters. Before the reaction, the sealing property of the photocatalytic activity evaluation system was detected, and the results showed that it was good . In the experiment, the internal circulation reactor was first evacuated, washed three to five times with high-purity CO_2 gas, and the impurity gas in the system was removed through switch control. Next, adjust the catalytic environment and fill the circulating reactor with high-purity CO_2 gas to control the pressure at 0.08 atmospheres. Finally, it sits for a time (about 1 hour) to form an environment saturated steam with carbon dioxide. The catalysate CO, CH_4 and hydrocarbon gaseous products at different reaction times were automatically detected by an online gas chromatograph, which was equipped with an automatic flame ionization detector (FID). Then, the stability of pure g-C_3N_4, $CsPbBr_3/CsPb_2Br_5$, and gCN0D/2D composite of samples were tested for consecutive photoreaction runs of 8 h in each run.

2.9 Theoretical model calculation

The spin-polarized density functional theory (DFT) calculations were performed by Vienna Ab Initio Simulation Package. The projector augmented wave (PAW) approach was applied to describe electron-ion interaction. The generalized gradient approximation and Perdew-Burke-Ernzerhof functional (GGA-PBE) were used, and a cutoff energy of 520 eV was employed. Optimized structures were obtained when total energy change and the maximum forces on all ions were less than 10^{-4} eV and -0.05 eV/Å, respectively. The Gaussian smearing method with a width of 0.05 eV was used to improve the convergence and treat the electron exchange and correlation energies. The surface Brillouin was sampled at the Γ-point. The climbing image nudged elastic band (CI-NEB) approach was employed to locate the transition state.

The g-C_3N4 (100) surface was modeled by a 1 × 1 supercell slab model containing 275 atoms. A 15 Å vacuum gap separated the neighboring slabs in the z direction to avoid their interactions. During geometry optimization, all-layer atoms were relaxed. 0D/2D homologous heterojunction $CsPbBr_3/CsPb_2Br_5$ surface was also modeled by a 1 × 1 supercell slab model. The adsorption energy for the adsorbate on the catalyst model surface was calculated using Eq. (1):

$$\Delta E\text{ads}=E(\text{Adsorbate/Surface})-E(\text{Adsorbate})-E(\text{Surface}) \quad (1)$$

where E(Adsorbate/Surface) is the total energy of the surface with the adsorbate, E(Adsorbate) and E(Surface) represent the energies of the free adsorbate molecule CO_2 in the gas phase and the clean surface, respectively.

All the H_2O, CO, CH_4, CO_2, and N_2 were calibrated depending on the standard gas to determine the peak position, calibration factor, and retention time. The calculation details of CO_2 conversion, product selectivity, and space-time yield (STY) can be found in the following equations.

The conversion of CO_2 (XCO$_2$) was calculated in Eq. (2):

$$X_{CO_2}(100\%) = \frac{[\mathrm{CO_2}]_{\mathrm{in}} - [\mathrm{CO_2}]_{\mathrm{out}}}{[\mathrm{CO_2}]_{\mathrm{in}}} \times 100\% \quad (2)$$

where $[CO_2]_{in}$ and $[CO_2]_{out}$ represent the carbon molar concentrations of CO_2 (relative to N_2) in the inlet and outlet gas, respectively.

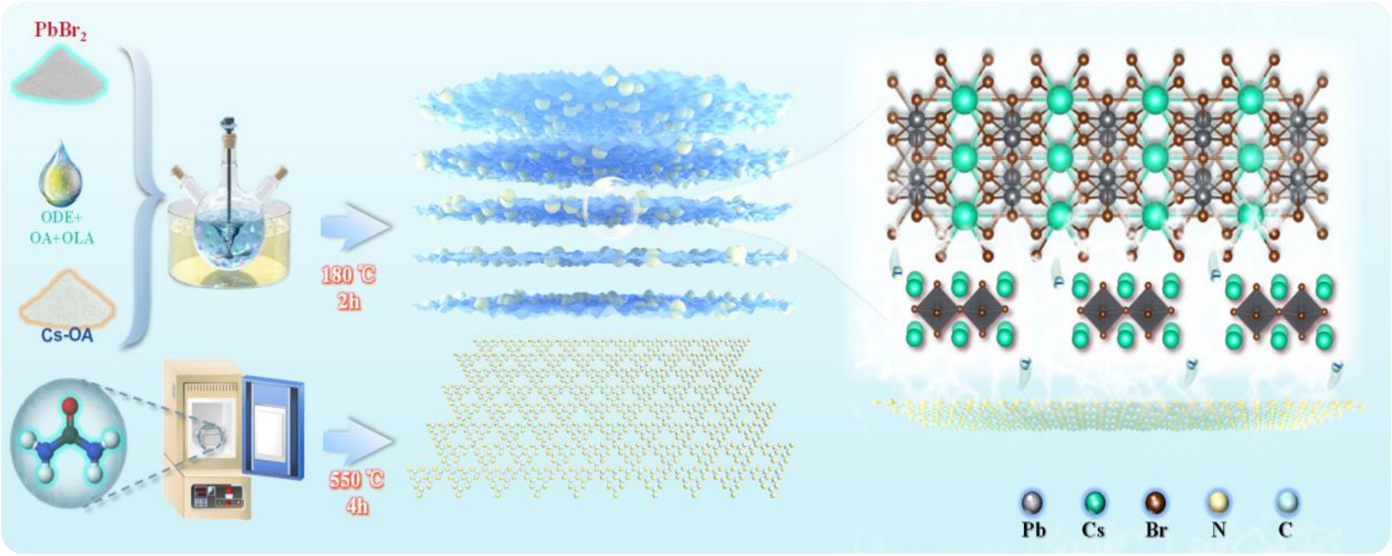

Fig. 1: Schematic illustration of the fabrication process of type I II heterojunction 2D/0D/2D g-C_3N_4/$CsPbBr_3$/$CsPb_2Br_5$ heterojunction.

CO selectivity (S_{CO}) and CH_4 selectivity (S_{CH_4}) was calculated using Eqs. (3) and (4):

$$S_{CO}(100\%) = \frac{[\mathrm{CO}]_{\mathrm{out}}}{[\mathrm{CO_2}]_{\mathrm{in}}-[\mathrm{CO_2}]_{\mathrm{out}}} \times 100\% \tag{3}$$

$$S_{CH_4}(100\%) = \frac{[CH_4]_{\mathrm{out}}}{[\mathrm{CO_2}]_{\mathrm{in}}-[\mathrm{CO_2}]_{\mathrm{out}}} \times 100\% \tag{4}$$

where $[CO]_{out}$ and $[CH_4]_{out}$ represent the carbon molar concentrations of CO and CH_4 in the outlet gas, respectively. The amount of CH_4 in our experiment was so small that we ignored it.

3. Results and discussion

The synthesis schematic of the type I-II homologous perovskite heterojunction 2D/0D/2D g-C_3N_4/$CsPbBr_3$/$CsPb_2Br_5$ is described in Fig. 1. Firstly, lead halide perovskite complex $CsPbBr_3$/$CsPb_2Br_5$ was synthesized by hot solvent injection. Then, the $CsPbBr_3$/$CsPb_2Br_5$ complex was generated in situ. The detailed synthesis steps are mentioned in the Experimental Section.

The morphologies of the prepared samples were characterized using Scanning Electron Microscope (SEM) and High-resolution TEM (HRTEM) techniques, as shown in Fig. 2 and (Figs. S3-4). HRTEM was performed to confirm the composition of the heterojunction compound (Fig. 2a). The SEM image (Fig. 2f) reveals a lamellar structure decorated with flocculent particles. Amorphous g-C_3N_4 is dispersed in the surface layer of the sample (Fig. 2a). HRTEM image with corresponding live Fast Fourier transformation (FFT) patterns (Fig. 2b) display 0D $CsPbBr_3$ and 2D $CsPb_2Br_5$ lattice signals. In Fig. 2b, lattice fringes with a d-spacing of 0.291 nm correspond to (220) panes of $CsPbBr_3$ QDs, while the lattice fringes with d-spacing of 0.421 nm correspond to (200) planes of $CsPb_2Br_5$. The angle measures 15°, indicating a near-location relationship between $CsPbBr_3$ and $CsPb_2Br_5$. EDS results (Fig. S4b) demonstrate that the mass fraction of each element in gCN0D2D-8 composites aligns with the proportion of the synthetic materials used. Energy-dispersive X-ray spectrometer mapping data (Fig. S2j-k, Fig. S4) reveals a uniform distribution of elements (C, N, Br, Pb, and Cs) throughout the nanocomposite structure. Based on the above characterizations, it is evident that the g-C_3N_4/$CsPbBr_3$/$CsPb_2Br_5$ heterojunction has been successfully formed.

The X-ray patterns of the synthesized samples are shown in Fig. 3a. The prepared g-C_3N_4 showed prominent peaks of (100) and (200) at 12.84° and 27.52°, respectively, which corresponds to the characteristic peaks of g-C_3N_4.[50] The XRD patterns of homologous perovskite $CsPbBr_3$/$CsPb_2Br_5$ (0D2D) heterojunction showed prominent peaks of (002), (100), (112), (202), (220), (211) and (420) at 11.81°, 15.41°, 19.01°, 23.58°, 29.56°, 37.94°, 48.05° respectively, which comes from zero-dimensional material $CsPbBr_3$ quantum dots including the (100), (202) and (211). The (002), (112), (220) and (420) come from the two-dimensional material $CsPb_2Br_5$. The characteristic peaks of both g-C_3N_4 (Fig. S1a) and $CsPbBr_3$/$CsPb_2Br_5$ still appeared clearly on the X-ray diffractograms of the g-C_3N_4/$CsPbBr_3$/$CsPb_2Br_5$ heterojunction with a different mass ratio and intensity. Fig. S1c shows the crystal plane attribution of 0D2D homologous perovskite, which is consistent with the composite material. The magnified XRD Fig. S1d shows that gCN0D2D-8 has the largest right shift of the lattice diffraction peak position, indicating a decrease in the unit cell constant. Above results indicated the successful preparation compound of g-C_3N_4/$CsPbBr_3$/$CsPb_2Br_5$ heterojunction.

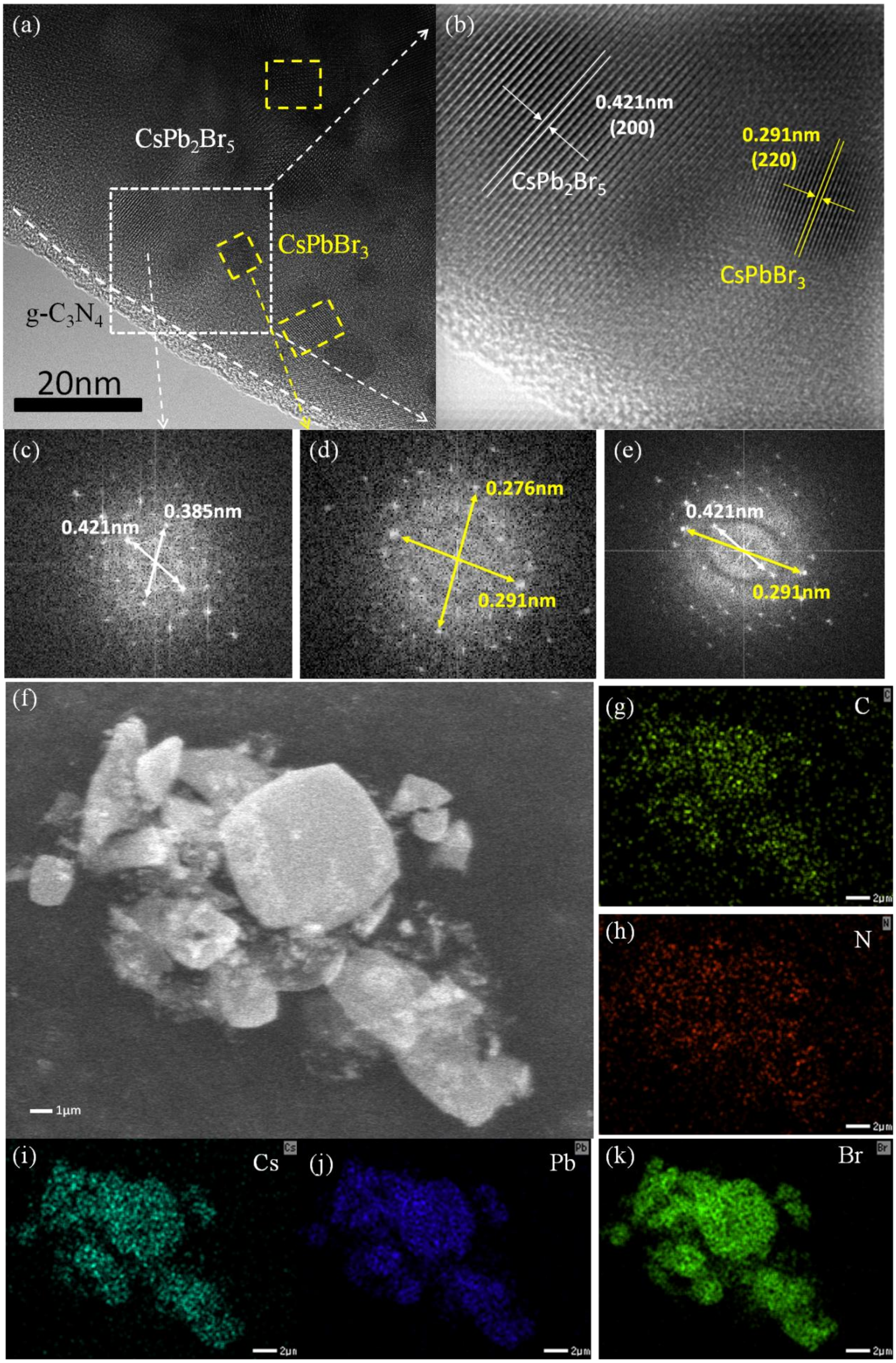

Fig. 2: Structural characterizations of gCN0D2D-8, (a)TEM image, (b-e) two-dimensional fast Fourier transformations (FFT) patterns, (f-k) EDS of g-C_3N_4/$CsPbBr_3$/$CsPb_2Br_5$ heterojunction.

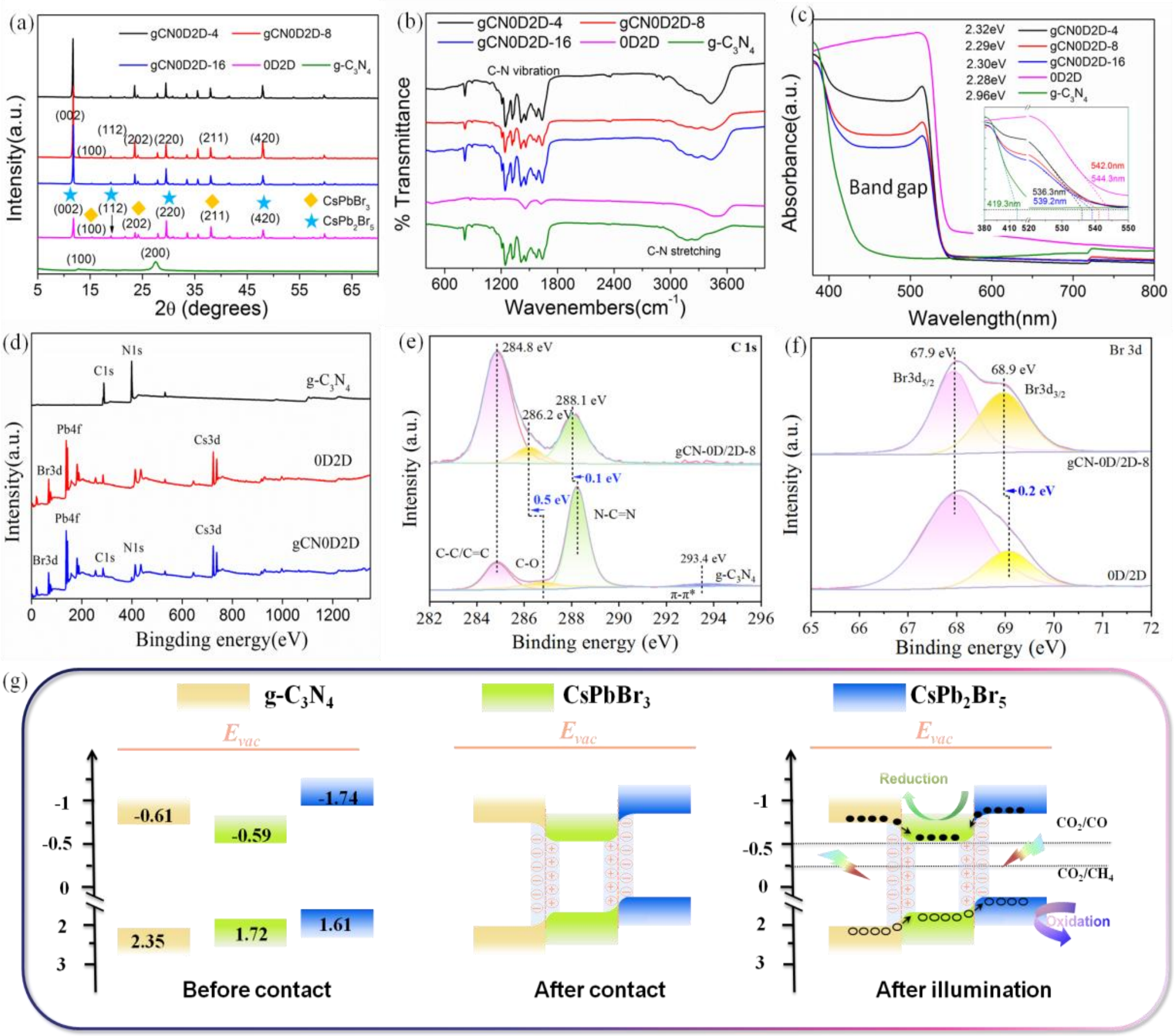

Fig. 3: (a) XRD patterns of samples, The FTIR (b) (c) UV-vis DRS of samples (d) The XPS survey spectra of the samples, display the presence of C, N, Br, Cs, and Pb in samples. (e) C 1s (f) Br 3d (g) band structures of the samples.

The FTIR spectra of g-C_3N_4, $CsPbBr_3$/$CsPb_2Br_5$(0D2D), and gCN0D2D photocatalysts are shown in Fig. 3b and Fig. S1b. The C–N and C=N stretching vibration modes can be seen at 1639.5 cm^{-1}, 1241.4 cm^{-1}, respectively. The out-of-plane bending vibration of the s-triazine ring displayed at 1320.4 and 1241.3 cm^{-1} (Fig. S1b). The molecule breathing modes of tris-triazine units also be displayed at 808.2 cm^{-1} while, the presence of impurity water molecules be displayed at 3182.5 cm^{-1}.[45] The asymmetric and symmetric Pb–Br stretching vibrations , as well as the bending vibrations of the 0D2D homologous perovskite Cs-Pb, were presented at 2920.2 cm^{-1}, 2852.7 cm^{-1}, and 1458.2 cm^{-1}.[26]

In the FTIR spectrum of the g-C_3N_4/$CsPbBr_3$/$CsPb_2Br_5$ heterojunction, in addition to the typical peaks, a clear blue shift in peak position 1240.3 cm^{-1} of in C–N stretching mode and the vibrational modes of tris-s-triazine units , then, the blue shift of the composite material gCN0D2D-8 is the largest, reaching 3cm^{-1}. The blue shift indicates a strong interaction between the g-C_3N_4 and homologous perovskite $CsPbBr_3$/$CsPb_2Br_5$(0D2D) interface,[2] which, leading to an increase in the electron density of gCN0D2D. Notably, even with a single molar ratio of 1:1, all g-C_3N_4 can be effectively incorporated onto the surface of homologous perovskite $CsPbBr_3$/$CsPb_2Br_5$(0D2D), forming a type I-II heterojunction structure.

In order to study the light-capturing property, UV-vis spectra were recorded, as shown in Fig. 3c. The absorption edge of g-C_3N_4, the homologous perovskite $CsPbBr_3$/$CsPb_2Br_5$(0D2D), and gCN0D2D series samples are observed around 419.3 nm, 536.3 nm, 539.2 nm, 542.0 nm, and 544.3 nm, respectively, corresponding to the band gap energy of approximately 2.96 eV, 2.28 eV, 2.30 eV, 2.29 eV, and 2.32 eV. All samples can be excited under simulated sunlight irradiation. Obviously, the band gap of the composite material changed under the modification of g-C_3N_4,[51] and this change is beneficial to the stability of the photocatalyst material.[52]

The bonding information of g-C_3N_4 and homologous heterojunction $CsPbBr_3/CsPb_2Br_5$, and composites was investigated using X-ray photoelectron spectroscopy (XPS) respectively (as shown in Fig. S3d,e,f and Fig. S5). We chose the 284.8eV of C as the calibration position. The C 1s spectrum of g-C_3N_4 is resolved into four peaks at 284.8, 286.7, 288.3, and 293.4eV, which are attributed to adventitious hydrocarbon, heptazine units, and N-C=N coordination in triazine rings, C-C interlayer vibration, respectively. Accordingly, the N 1s spectrum in g-C_3N_4 shows the existence of sp2-hybridized nitrogen in triazine rings (C-N=C) at 398.4 eV, tertiary nitrogen (N-$(C)_3$) at 400.3 eV, amino groups (C=N) at 401.2 eV and positive charge localization in heterocycles (C-N) at 404.2 eV, respectively.[45]

In Fig. 4d, Survey spectra of the samples show distinct binding energies about 284 eV, 398 eV, 68 eV, 140eV, 724eV, ascribed to C, N, Br, Pb, and Cs, indicating the successful synthesis of the composites of g-$C_3N_4/CsPbBr_3/CsPb_2Br_5$. After fitting the spectra, small binding energy shifts are observed in the typeI-II heterojunction composite structures compared to their individual components, such as C1s, N1s, Br3d, Cs3d, and Pb4f. These binding energy shifts indicate that there are close interactions within the structure, leading to the redistribution of charges. Consequently, g-C_3N_4 becomes electron-rich, while the homologous perovskite becomes electron-deficient, which is supported by the negative shift in the binding energy of N 1d in gCN0D2D-8. The binding energy of Br 3d (Fig. 3f) in the 0D2D is 68.1eV and 69.2 eV, corresponding to Br $3d_{5/2}$ and Br $3d_{3/2,}$ respectively. The offset of gCN0D2D-8 relative to 0D2D is 0.2eV, 0.2eV. The binding energy of Cs 3d (Fig. S5e) in the 0D2D shows two peaks at 723.5 eV and 737.5 eV, corresponding to Cs $3d_{5/2}$ and Cs $3d_{3/2}$. For gCN0D2D-8, the offset relative to 0D2D is 0.2 eV (723.5eV) and 0.2 eV (737.7eV). The binding energy of Pb 4f (Fig. S5f) in the 0D2D shows two peaks at 138.1eV and 143.0 eV, corresponding to Pb $4f_{7/2}$ and Pb $4f_{9/2}$. For gCN0D2D-8, the offset relative to 0D2D is 0.2 eV (138.3eV) and 0.2 eV (143.2eV), indicating an intense electron deficiency in the homologous perovskite. We also compared the XPS of the heterojunction formed by g-$C_3N_4/CsPb_2Br_5$, as shown in Fig. S5e-i, which formed a typeI heterojunction.

The valence band (V_B) potential can be determined by analyzing the the valence bands of g-C_3N_4, $CsPbBr_3$, and $CsPb_2Br_5$. As shown in Fig. S6, the energy level of the valence band maximum (V_{BM}) for g-C_3N_4, $CsPbBr_3$, and $CsPb_2Br_5$ is 2.24 eV, 1.55 eV, and 1.50 eV, respectively. Based on these results, the band structures of g-C_3N_4 , $CsPbBr_3$ and $CsPb_2Br_5$ can be derived with V_{BM} energies of 2.35 eV, 1.72 eV, and 1.61 eV, respectively. Consequently, the corresponding conduction band energies are -0.61 eV, -0.59eV and -1.74eV respectively. The conduction band minimum of g-C_3N_4 is 0.02 eV and 1.62

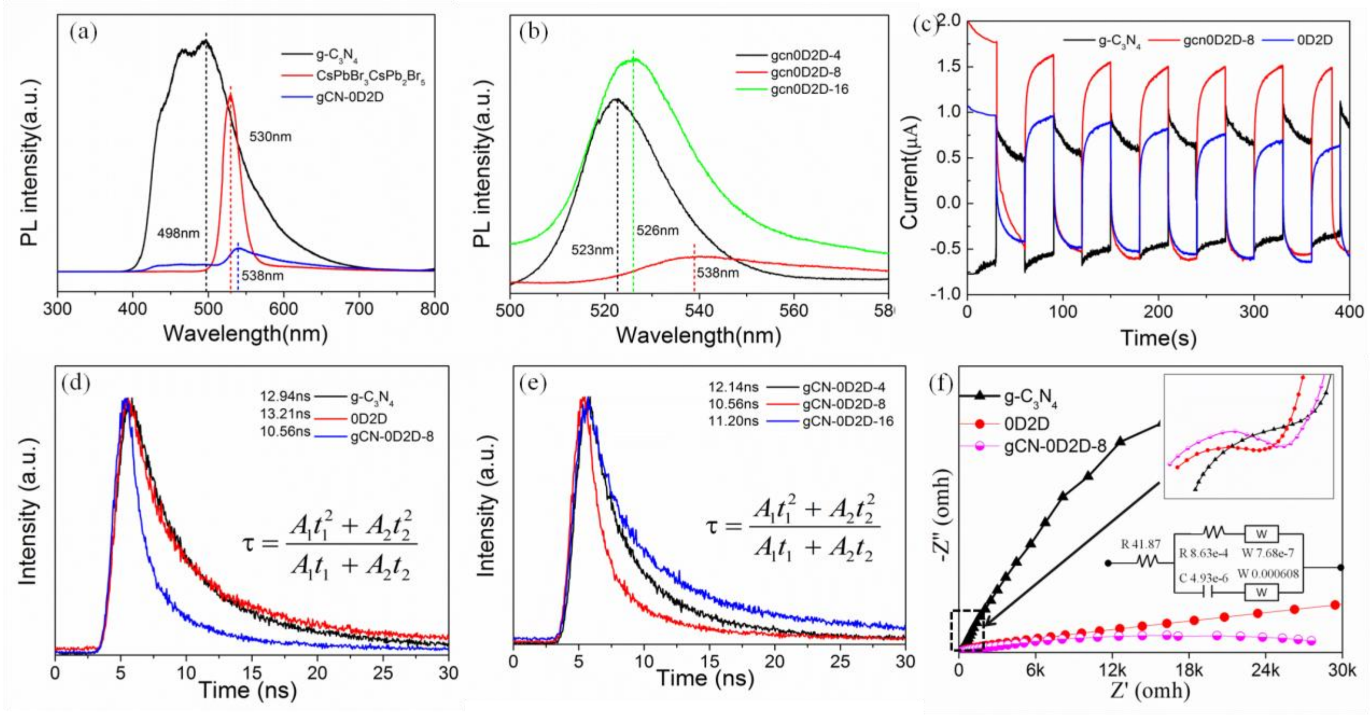

Fig. 4: (a) (b) PL spectra, (d) (e) Time-resolved transient PL decay curves, (c) Transient photocurrent responses density versus time (i-t curve) and (f) EIS spectra of samples.

eV lower than that of them. These data provide insights into the band structure of g-C_3N_4, $CsPbBr_3$ and $CsPb_2Br_5$ (Fig. 3g). Obviously, homologous perovskite 0D2D can form typeII heterojunctions. When g-C_3N_4 is contacted, type I heterojunctions are formed between g-C_3N_4 and $CsPbBr_3$. Thus, Type I-II heterojunctions are formed among g-C_3N_4, $CsPbBr_3$ and $CsPb_2Br_5$.

Photoluminescence (PL) is used to study the light absorption of photocatalysts and the transition between energy levels. Among these, the luminescence intensity indicates the rate of photo-induced electron-hole pair recombination. A lower luminescence intensity suggests that the recombination has been strongly suppressed. As shown in Fig. S4a-b, it can be observed that pure g-C_3N_4 and $CsPbBr_3$/$CsPb_2Br_5$ (0D2D) heterojunction exhibit strong and broad PL emission absorption at wavelengths of approximately 498 nm and 530 nm, respectively, which is consistent with the description in reference.[24] However, the PL peak intensity of the gCN0D2D heterojunction is significantly quenched compared to pure g-C_3N_4 and $CsPbBr_3$/$CsPb_2Br_5$ samples. Compared with other composite material samples, the emission intensity of gCN0D2D-8 is the lowest, and the excitation wavelength has increased, which indicates that the band gap of the material has become smaller. Table S1 presents the time-decay PL spectral fitting lifetimes of each catalyst. The intervention of g-C_3N_4 makes the composite construct a double type I-II heterojunction, effectively inhibiting the photogenerated carrier recombination in the heterojunction.

Time-resolved fluorescence attenuation techniques are often used to study photocatalysts' charge transfer and separation behavior.[53] As shown in Fig. S4d-e, and Table S1, all samples rapidly decay within the nanosecond timescale. The average emission lifetime of g-C_3N_4, $CsPbBr_3$/$CsPb_2Br_5$ (0D2D) heterojunction, and gCN0D2D are 12.94 ns, 13.21 ns, and 10.56 ns, respectively. In the experiment, the reduction of emission lifetime indicates that the charge separation ability is enhanced and the charge recombination opportunity is reduced, which is conducive to improving photocatalytic performance. In the three gCN0D2D samples, their lifetimes are 12.14 ns, 10.56 ns, and 11.20 ns, respectively. The lifetime of the gCN0D2D-8 sample is the smallest, so it can transfer charges quickly.

To further understand the photogenerated carrier transfer efficiency and separation efficiency,[54] we performed transient photocurrent measurements (Fig. 4c and Fig. S9), and in all samples we tested, gCN0D2D-8 showed higher photocurrent, indicating enhanced carrier separation and transfer. The recombination of g-C_3N_4 is thought to facilitate the efficient separation of photo-excited electrons and holes. The catalytic activity of the samples was studied by electrochemical impedance spectroscopy (EIS), including g-C_3N_4, 0D2D heterojunction, and gCN0D2D heterojunction, as shown in Fig. 4f. The arc radius of g-C_3N_4 and 0D2D perovskite composites is much larger than that of gCN0D2D-8 heterojunction composite material. It can be seen from Fig. 4c, gCN0D2D-8 has the smallest arc radius, indicating a reduced electrical impedance and enhanced charge transfer. The minor resistance range (as shown in the in the enlarged part of Fig. 4f) also shows a more minor arc, meaning reduced resistance and enhanced charge transfer. The equivalent circuit diagram of gCN0D2D-8 also shows a smaller impedance during the generation of photocurrent. The increase in electrical conductivity and charge transfer of 0D2D perovskite composites is caused by the modification of g-C_3N_4, which also belongs to the kinetic category of the catalyst.

In our photocatalytic experiments, CO is the main product, accompanied by a small amount of CH_4. Moreover, there is almost no CH_4 product when the gCN0D2D samples is used for photocatalytic reduction of CO_2.[55-57] The photocatalytic CO_2 reduction activity is assessed in a photocatalytic closed system simulating sunlight and CO_2 saturated water vapor (Fig. S11). We first conducted a controlled experiment without simulating sunlight, and CO_2 did not show any detectable CO, CH_4, H_2, and others hydrocarbon without any photocatalyst, which confirmed the necessity and importance of catalysts in the photocatalytic process of CO_2 reduction. The photocatalytic yields of a single g-C_3N_4, including CO and CH_4, can reach 6.36 μmol g^{-1} h^{-1} and 0.12 μmol g^{-1} h^{-1}. We have studied the photocatalytic properties of 0D2D perovskite composites with different proportions. The results show that CO dominated the product, while CH_4 was almost negligible. When $CsPbBr_3$ and $CsPb_2Br_5$ are in the ratio of 1:1, the photocatalytic properties are better, reaching 6.23 μmol g^{-1} h^{-1}, which is close to the photocatalytic properties of g-C_3N_4. The gCN0D2D composite obtained by combining with g-C_3N_4 has excellent properties. Among the samples, gCN0D2D-8 has the highest CO yield of 28.46 μmol g^{-1} h^{-1}, about 4.5 times and 4.6 times higher than pure g-C_3N_4 and 0D2D complex. The significant increase in CO production highlights the feasibility of constructing double-type II heterojunction nanocomposites.

The photocatalytic performance of the heterojunction of a single perovskite complex with different proportions is similar to that of $CsPbBr_3$ quantum dots and two-dimensional $CsPb_2Br_5$, as shown in Fig. 5a, indicating that $CsPbBr_3$ and $CsPb_2Br_5$ do not form a good heterojunction structure. This result is consistent with EIS and photocurrent measurements and previous reports, and adjusting the proportion of components has little effect on photocatalytic performance. In the 0D2D perovskite photocatalyst, the sample of 1:1 components showed relatively good performance, but due to defects, the photocatalytic performance of this heterojuncti on was not satisfactory. After adding g-C_3N_4, a type I-II heterojunction was formed, which made up for the defect and improved the performance of the photocatalyst. With the increase of g-C_3N_4, the maximum photocatalytic performance was achieved in gCN0D2D-8, and the CO yield was increased by more than 4 times. However, with the further increase of g-C_3N_4, the photocatalytic performance of the composite began to decline, but it was still better than all 0D2D perovskite

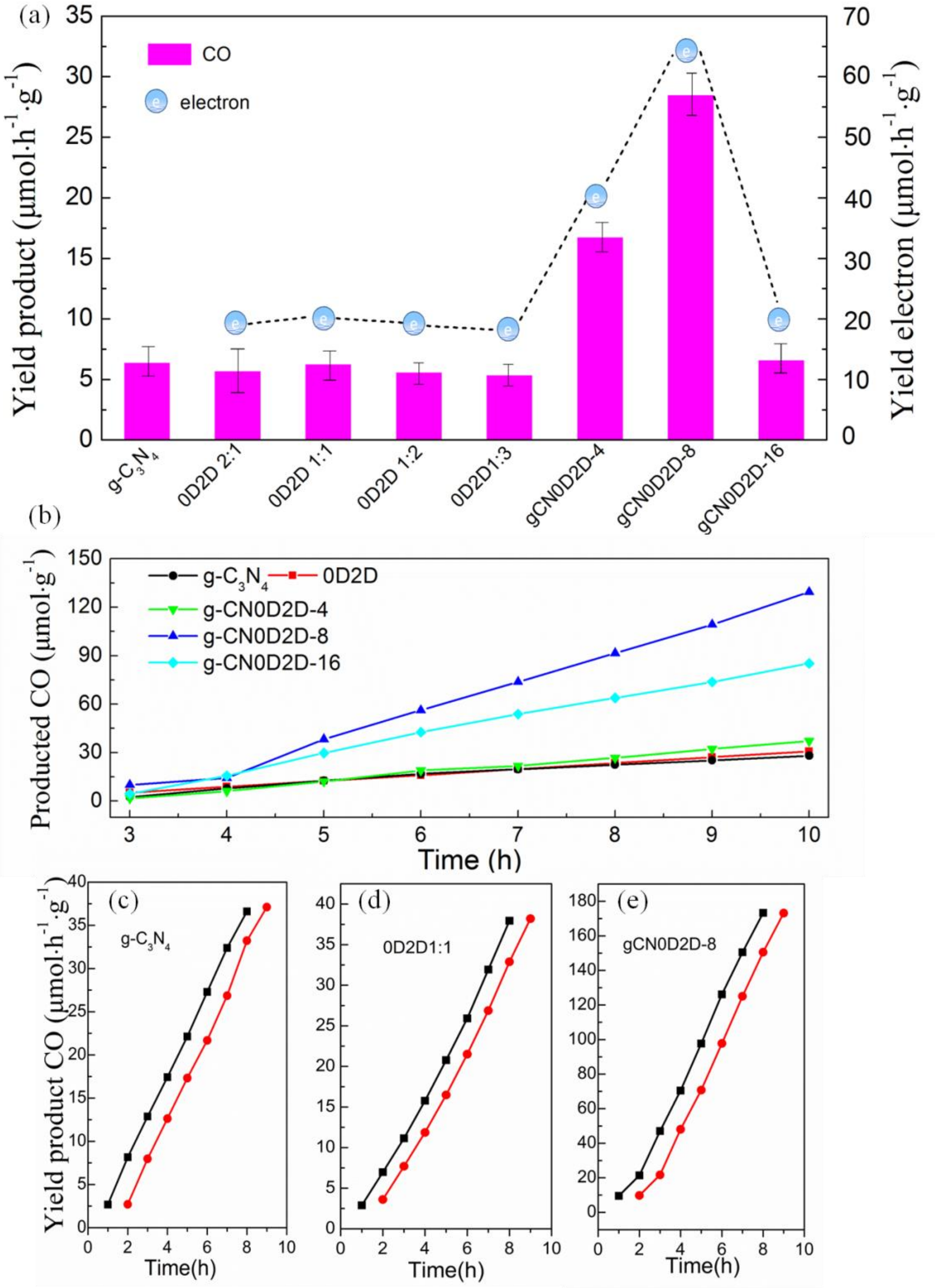

Fig. 5: (a) Comparison of the total product and electron yields of the different samples (b) The CO yield every hour under light irradiation. (c), (d) and (e) Repeatability experiment of CO yield.

binary photocatalysts. It shows that nitrogen carbide has good electrical properties and promotes charge transfer of 0D2D perovskite heterojunction, as supported by PL and TRPL characterization. The experimental results show that the CO yield is 28.17 μmol g^{-1}h^{-1}, and the photocatalytic performance is the best, exceeding most previous studies. The relevant literature reported by predecessors is shown in Table 1. The catalytic rate of CO on gCN0D2D-8 has apparent advantages.

From a thermodynamic point of view, the reduction potential for reducing CO_2 and H_2O to CO and CH_4 requires -0.53V ($CO_2 + 2\ H^+ + 2\ e^- \rightarrow CO + H_2O$, -0.53 V/NHE) and -0.24V ($CO_2 + 8\ H^+ + 8\ e^- \rightarrow CH_4 + 2\ H_2O$, -0.24 V/NHE). Our theoretical calculations provide a graph illustrating all possible ways carbon dioxide is reduced to CO, CH_4, and other products. The product CO is thought to be obtained by a redox reaction, where our type I-II heterosynthesis provides the necessary photocatalytic energy for the generation of CO. On the other hand, the product CH_4 is also formed by REDOX, including the transfer of four electrons and the CO of the intermediate. When the reduction potential of the electronic system of the system is low, the thermodynamic reaction rate of the element will decrease. Therefore, after CO formation, subsequent photocatalytic reactions may absorb photogenerated carriers on the surface of the photocatalyst. This results in CO being the main product, CH_4 being a by-product, and even CH_4 not being produced.

Table 1: Comparison CO evolution rates of the prepared photocatalyst with other literature.

Photocatalyst	Light source	Solvents	CO evolution ($\mu mol/g^{-1}h^{-1}$)	Ref.
PCN $CsPbBr_3$ CPB-PCN	300 W Xe-lamp	acetonitrile/water Ethyl acetate/water	52 9.8 149.	[2]
$CsPbBr_3$ NCs $CsPbBr_3$ NCs/GO	100 W Xe lamp	Ethyl acetate	4.12 4.89	[12]
CPB-CN	300 W Xe-lamp (>420 nm)	CO_2 and water vapor	11.5	[58]
$CsPbBr_3$ $CsPb_2Br_5$ $CsPbBr_3/CsPb_2Br_5$	300 W Xe-lamp (>420 nm)	CO_2 and water vapor	78.844 179.19 197.11	[24]
$g\text{-}C_3N_4$ $CsPbBr_3$ $g\text{-}C_3N_4$/ $CsPbBr_3$ /$CsPb_2Br_5$	300 W Xe-lamp (>420 nm)	CO_2 and water vapor	6.26 6.13 28.17	This work

We conducted repetitive tests, and each test lasts 5 hours. As shown in Fig. S5(c-e) and Fig. S8, the maximum loss of activity of the photocatalyst was only 8%, indicating that the photocatalytic activity of the materials is very stable. XRD and FTIR spectra of 0D2D and gCN0D2D samples fresh and used the stability test are shown in Fig. S20. The crystal structure and chemical functional groups did not change significantly before and after catalysis. Among them, after catalysis, for perovskite $CsPbBr_3$, the (100) and (202) crystal planes are enhanced, while the (002), (112) and (220) crystal plane strengths of $CsPb_2Br_5$ are weakened, and the (300) crystal plane strength increases, which indicating that the photocatalyst was relatively stable relative to the reaction conditions.

Theoretical calculation and simulation analysis of materials are conducive to exploring the dynamics and internal mechanisms of the system.[59,60] Therefore, conducting the numerical simulation and carrying out application practice have significant practical significance.[61-65] Density functional theory (DFT) predicts the electronic structure of matter by studying the electron density. Since it was proposed by John Pople, Martin Karplus and others in the 1960s, DFT has been widely applied in fields such as materials science, chemistry and physics. For our material model, the (100) surface orientation of $g\text{-}C_3N_4$ and $CsPbBr_3/CsPb_2Br_5$ (0D2D) materials were selected as the model to simulate the density of state (DOS) and charge density difference.[66,67] Since photocatalysis mainly occurs with the catalyst on the surface, when constructing the heterojunction, we consider $g\text{-}C_3N_4$ with four different 0D2D homologous perovskite structures, including CN-CsBr-CsBr, CN-CsBr-PbBr, CN-PbBr-CsBr and CN-PbBr-PbBr, as shown in Figs. 6c,d,g,h. In the type I-II heterojunction, the conduction band is dominated by Cs, composed of empty 3d orbitals. On the other hand, the valence band consists of orbitals of the N and Br elements. It is confirmed that $g\text{-}C_3N_4$ can modify the band structure of 0D2D perovskite homologous heterojunction. The total DOS of the (100) crystal face is shown in Fig. S15a-d. There is a bandgap shift near the Fermi level of the composite material, indicating that the electrical conductivity is improved, which means that the transport performance of electrons can be enhanced, helping to improve its photocatalytic performance.

In order to better understand the electronic properties of the interface between $g\text{-}C_3N_4$ and 0D2D perovskite materials, we calculate the three-dimensional charge density difference and the plane-average electrostatic potential drop at the interfaces. For 0D2D perovskite binary heterojunction interface, CsBr-CsBr, CsBr-PbBr, PbBr-CsBr, and PbBr-PbBr (Fig. S16 and S17), the electrostatic potential and potential difference are 0.78 eV, 0.78 eV, 1.26 eV, and 1.41eV, respectively (Fig. S18). The first two directions are from $CsPbBr_3$ to $CsPb_2Br_5$, and the last two are from $CsPb_2Br_5$ to $CsPbBr_3$. The internal electric field generated by the potential difference is not in the same direction as the heterostructure. Therefore, the 0D2D $CsPbBr_3/CsPb_2Br_5$ material has a natural deficiency in photocatalysis. After $g\text{-}C_3N_4$ adding modification, the electrostatic potential and potential difference of the system are shown in Fig. S14a-c. The internal electric field generated by the potential difference is in the same direction as the heterostructure.[68] Photoelectrons drift from $g\text{-}C_3N_4$ to $CsPbBr_3$ to the $CsPb_2Br_5$ surface, while light-generated holes tend to drift in the opposite direction. This trend favors the separation and transfer of photogenic carriers and promotes the enhancement of photocatalytic performance. For gCN0D2D material heterojunction interface, CN-CsBr-CsBr, CN-CsBr-PbBr, CN-PbBr-CsBr and CN-PbBr-PbBr, the electrostatic potential and potential difference of the four different structures from $g\text{-}C_3N_4$ to $CsPbBr_3$ to the $CsPb_2Br_5$ are 0.84 eV and 0.31eV, 0.65eV and 2.75 eV, 0.51 eV and 2.82 eV, 1.71 eV and 2.25 eV, respectively. These values are more significant than the electrostatic potential difference of the 0D2D perovskite heterojunction. The total DOS (Fig. S17a-f) of the 0D2D perovskite heterojunction shows a relatively large band gap reflecting the energy difference between the valence and conduction bands.

However, the total DOS (Fig. S15a-f) shows a relatively small band gap. Hence, the energy difference between the valence and conduction bands is relatively small, which is conducive to the separation and transfer of photogenic carriers. The charge difference of four different combinations in perovskite is shown in Fig. S10. Theoretical calculation shows that CN-CsBr-PbBr and CN-PbBr-CsBr show lower binding energies in the binding, which are -1603.774eV and -1481.12926eV, respectively, which means that our structure is more inclined to these two compositions. Therefore, when we consider the adsorption of CO_2 at the heterojunction interface, We only chose these two, as shown in Fig. S11. The involvement of g-C_3N_4 lowers the adsorption energy of the

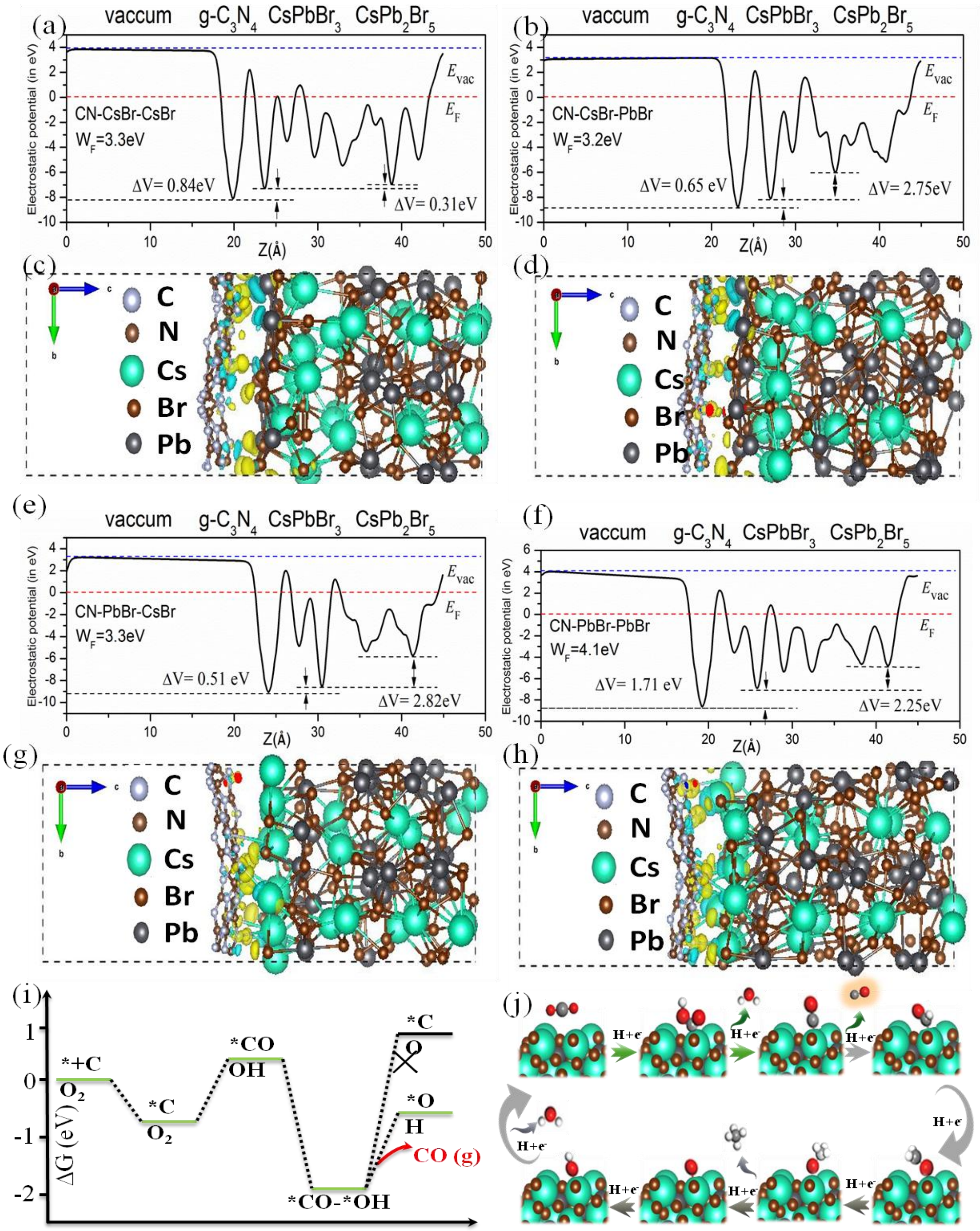

Fig. 6: (a, b, e, f) is the work function of the heterojunction. c, d, g, h 3D charge density difference and the planeaveraged electrostatic potential drop across the interface of the CsPbBr3, E_F, and $E_v$ac represent Fermi level and vacuum level, respectively. i,j is Gibbs free energy and product process.

composite than that of the homologous perovskite composite, corresponding to the more favorable application of photocatalysis.

4. Conclusions

In summary, the g-C_3N_4/$CsPbBr_3$/$CsPb_2Br_5$ structure of the type I-II heterojunction was successfully synthesized by modifying the homologous perovskite heterojunction with g-C_3N_4 and using the physical composite method. The photocatalytic performance was significantly improved through interfacial band matching and interinternal electric field adjustment, and the CO production rate reached 28.17 μmol g^{-1} h^{-1}, which was a substantial enhancement compared with the single g-C_3N_4 and $CsPbBr_3$/$CsPb_2Br_5$ dual structures. Lattice matching homologous perovskite heterojunctions have been observed in type I-II heterojunctions. This interaction contributes to the transfer of electrons and the reduction of charge recombination, resulting in better photocatalytic activity to reduce CO_2 to CO. Both experiments and theoretical calculations confirm the existence of an internal electrostatic field, which promotes the transfer of electrons and enhances the efficiency of photocatalysis. This practice provides new insights into the design of heterogeneous nanocomposite photocatalysts with perovskite complexes

Acknowledgements

This work was supported by the National Natural Science Foundation of China (Grant Nos, 12204014), the Science and Technology Planning Project of Henan Province (No. 232102241016). It is funded by the Natrual Science Foundation of Henan Province (No. 252300420018), the Energy Power university-level key discipline of Anyang Institute of Technology. The National Natural Science Foundation of China (Grant No. 12381240132), the Postgraduate Education Reform and Quality Improvement Project of Henan Province (Grant No. YJS2023JD60).

Conflict of Interest

There is no conflict of interest.

Supporting Information

Applicable.

CRediT Statement

Shiding Zhang completed all the experiments and tests, and wrote the main manuscript text. **Yuhua Wang** reviewed the experiments and manuscript and provided some useful and practical recommendations. **Sri Hari Kumar Annamareddy** reviewed the feasibility of the experiment and the theoretical calculations. **Yao Guo** did the VASP calculation and simulation. **Yitong Wang** wrote experiment project administration and all the figure and figure S. All authors reviewed the manuscript. **Haijun Zhang** put forward very good suggestions on the preparation and optimization of catalyst materials.

References

[1] W. Xie, K. Li, X.-H. Liu, X. Zhang, H. Huang, P-mediated Cu-N_4 sites in carbon nitride realizing CO_2 photoreduction to C_2H_4 with selectivity modulation, *Advanced Materials*, 2023, **35**, e2208132, doi: 10.1002/adma.202208132.

[2] M. Ou, W. Tu, S. Yin, W. Xing, S. Wu, H. Wang, S. Wan, Q. Zhong, R. Xu, Amino-assisted anchoring of $CsPbBr_3$ perovskite quantum dots on porous g-C_3N_4 for enhanced photocatalytic CO_2 reduction, *Angewandte Chemie International Edition*, 2018, **57**, 13570-13574, doi: 10.1002/anie.201808930.

[3] J. Gong, C. Li, M. R. Wasielewski, Advances in solar energy conversion, *Chemical Society Reviews*, 2019, **48**, 1862-1864, doi: 10.1039/c9cs90020a.

[4] S. Zhang, Y. Wang, G. A. M. Mersal, A. Alhadhrami, D. A. Alshammari, Y. Wang, H. Algadi, H. Song, Enhanced photocatalytic CO_2 reduction *via* MXene synergism: constructing an efficient heterojunction structure of g-C_3N_4/Nb2C/$CsPbBr_3$, *Advanced Composites and Hybrid Materials*, 2024, **7**, 226, doi: 10.1007/s42114-024-01026-x.

[5] X. Wen, X. Wu, L. Hu, X. Wu, H. Guo, B. Qian, Z. Liu, H. Li, Z. Fei, A critical review on modification strategies of $Bi_2Sn_2O_7$ photocatalysts and their applications in energy and environmental remediation fields, *Coordination Chemistry Reviews*, 2025, **526**, 216377, doi: 10.1016/j.ccr.2024.216377.

[6] M. D. Burkart, N. Hazari, C. L. Tway, E. L. Zeitler, Opportunities and challenges for catalysis in carbon dioxide utilization, *ACS Catalysis*, 2019, **9**, 7937-7956, doi: 10.1021/acscatal.9b02113.

[7] K. Ren, S. Yue, C. Li, Z. Fang, K. A. M. Gasem, J. Leszczynski, S. Qu, Z. Wang, M. Fan, Metal halide perovskites for photocatalysis applications, *Journal of Materials Chemistry A*, 2022, **10**, 407-429, doi: 10.1039/d1ta09148d.

[8] A. Mishra, R. Bose, Y. Zheng, W. Xu, R. McMullen, A. B. Mehta, M. J. Kim, J. W. P. Hsu, A. V. Malko, J. D. Slinker, Stable and bright electroluminescent devices utilizing emissive 0D perovskite nanocrystals incorporated in a 3D $CsPbBr_3$ matrix, *Advanced Materials*, 2022, **34**, e2203226, doi: 10.1002/adma.202203226.

[9] J. Zeng, X. Li, Y. Wu, D. Yang, Z. Sun, Z. Song, H. Wang, H. Zeng, Space-confined growth of $CsPbBr_3$ film achieving photodetectors with high performance in all figures of merit, *Advanced Functional Materials*, 2018, **28**, 1804394, doi: 10.1002/adfm.201804394.

[10] S. M. Kobosko, J. T. DuBose, P. V. Kamat, Perovskite

photocatalysis. methyl viologen induces unusually long-lived charge carrier separation in $CsPbBr_3$ nanocrystals, *ACS Energy Letters*, 2020, **5**, 221-223, doi: 10.1021/acsenergylett.9b02573.

[11] N. Li, X. Chen, J. Wang, X. Liang, L. Ma, X. Jing, D. Chen, Z. Li, ZnSe nanorods–$CsSnCl_3$ perovskite heterojunction composite for photocatalytic CO_2 reduction, *ACS Nano*, 2022, **16**, 3332-3340, doi: 10.1021/acsnano.1c11442.

[12] Y. Xu, M. Yang, B. Chen, X. Wang, H. Chen, D.-B. Kuang, C. Su, A $CsPbBr_3$ perovskite quantum dot/graphene oxide composite for photocatalytic CO_2 reduction, *Journal of the American Chemical Society*, 2017, **139**, 5660-5663, doi: 10.1021/jacs.7b00489.

[13] I. Dursun, M. De Bastiani, B. Turedi, B. Alamer, A. Shkurenko, J. Yin, A. M. El-Zohry, I. Gereige, A. AlSaggaf, O. F. Mohammed, M. Eddaoudi, O. M. Bakr, $CsPb_2Br_5$ single crystals: synthesis and characterization, *ChemSusChem*, 2017, **10**, 3746-3749, doi: 10.1002/cssc.201701131.

[14] K. M. Lytle, E. L. Brass, B. J. Roman, M. T. Sheldon, Thermal activation of anti-stokes photoluminescence in $CsPbBr_3$ perovskite nanocrystals: the role of surface polaron states, *ACS Nano*, 2024, **18**, 18457-18464, doi: 10.1021/acsnano.4c03548.

[15] G. Li, H. Wang, Z. Zhu, Y. Chang, T. Zhang, Z. Song, Y. Jiang, Shape and phase evolution from $CsPbBr_3$ perovskite nanocubes to tetragonal CsPb2Br5 nanosheets with an indirect bandgap, *Chemical Communications*, 2016, **52**, 11296-11299, doi: 10.1039/C6CC05877A.

[16] X. Yu, Z. Liu, X. Yang, Y. Wang, J. Zhang, J. Duan, L. Liu, Q. Tang, Crystal-plane controlled spontaneous polarization of inorganic perovskite toward boosting triboelectric surface charge density, *ACS Applied Materials & Interfaces*, 2021, **13**, 26196-26203, doi: 10.1021/acsami.1c05796.

[17] A. Swarnkar, R. Chulliyil, V. K. Ravi, M. Irfanullah, A. Chowdhury, A. Nag, Colloidal $CsPbBr_3$ perovskite nanocrystals: luminescence beyond traditional quantum dots, *Angewandte Chemie (International Ed)*, 2015, **54**, 15424-15428, doi: 10.1002/anie.201508276.

[18] L. Xu, Y. Yang, W. Wu, C. Wei, G. Luo, Z. Huang, W. Chen, H. Peng, Photoelectrochemical performance of ligand-free CsPb2Br5 perovskites, *Inorganic Chemistry Frontiers*, 2022, **9**, 4548-4553, doi: 10.1039/D2QI01085B.

[19] D. A. Roberts, B. S. Pilgrim, J. R. Nitschke, Covalent post-assembly modification in metallosupramolecular chemistry, *Chemical Society Reviews*, 2018, **47**, 626-644, doi: 10.1039/C6CS00907G.

[20] J. Yin, G. H. Ahmed, O. M. Bakr, J. L. Brédas, O. F. Mohammed, Unlocking the effect of trivalent metal doping in all-inorganic $CsPbBr_3$ perovskite, *ACS Energy Letters*, 2019, **4**, 789-795, doi: 10.1021/acsenergylett.9b00209.

[21] J. T. Mulder, I. du Fossé, M. Alimoradi Jazi, L. Manna, A. J. Houtepen, Electrochemical p-doping of $CsPbBr_3$ perovskite nanocrystals, *ACS Energy Letters*, 2021, **6**, 2519-2525, doi: 10.1021/acsenergylett.1c00970.

[22] X. Yu, L. Wu, D. Yang, M. Cao, X. Fan, H. Lin, Q. Zhong, Y. Xu, Q. Zhang, Hydrochromic $CsPbBr_3$ nanocrystals for anti-counterfeiting, *Angewandte Chemie International Edition*, 2020, **59**, 14527-14532, doi: 10.1002/anie.202005120.

[23] Z. Chen, Y. Hu, J. Wang, Q. Shen, Y. Zhang, C. Ding, Y. Bai, G. Jiang, Z. Li, N. Gaponik, Boosting photocatalytic CO_2 reduction on $CsPbBr_3$ perovskite nanocrystals by immobilizing metal complexes, *Chemistry of Materials*, 2020, **32**, 1517-1525, doi: 10.1021/acs.chemmater.9b04582.

[24] L. Ding, B. Borjigin, Y. Li, X. Yang, X. Wang, H. Li, Assembling an affinal 0D $CsPbBr_3$/2D $CsPb_2Br_5$ architecture by synchronously *in situ* growing $CsPbBr_3$ QDs and $CsPb_2Br_5$ nanosheets: enhanced activity and reusability for photocatalytic CO_2 reduction, *ACS Applied Materials & Interfaces*, 2021, **13**, 51161-51173, doi: 10.1021/acsami.1c17870.

[25] K. Xie, S. Wei, A. Alhadhrami, J. Liu, P. Zhang, A. Y. Elnaggar, F. Zhang, M. H. H. Mahmoud, V. Murugadoss, S. M. El-Bahy, F. Wang, C. Li, G. Li, Synthesis of $CsPbBr_3$/$CsPb_2Br_5$@silica yolk-shell composite microspheres: precisely controllable structure and improved catalytic activity for dye degradation, *Advanced Composites and Hybrid Materials*, 2022, **5**, 1423-1432, doi: 10.1007/s42114-022-00520-4.

[26] T. Paul, D. Das, B. K. Das, S. Sarkar, S. Maiti, K. K. Chattopadhyay, $CsPbBrCl_2$/g-C_3N_4 type II heterojunction as efficient visible range photocatalyst, *Journal of Hazardous Materials*, 2019, **380**, 120855, doi: 10.1016/j.jhazmat.2019.120855.

[27] C. Wan, Z. Wang, H. Zhang, S. Tie, Z. Liang, H. Xu, Y. Ma, Z. Wang, X. Zheng, X. Pan, J. Ye, Out-of-phase articulation strategy of $CsPbBr_3$/$CsPb_2Br_5$ perovskite for high sensitivity X-ray detection, *Advanced Functional Materials*, 2024, **34**, 2401220, doi: 10.1002/adfm.202401220.

[28] S. Phil, Optimizing surface passivation, *Science*, 2019, **366**, 1467, doi: 10.1126/science.366.6472.1467-e.

[29] J. Hu, P. Chen, D. Luo, L. Dai, N. Chen, S. Li, S. Yang, Z. Fu, D. Wang, Q. Gong, S. D. Stranks, R. Zhu, Z.-H. Lu, Anchoring of halogen-cleaved organic ligands on perovskite surfaces, *Energy & Environmental Science*, 2022, **15**, 5340-5349, doi: 10.1039/d2ee02698h.

[30] W. Qi, X. Zhou, J. Li, J. Cheng, Y. Li, M. J. Ko, Y. Zhao, X. Zhang, Inorganic material passivation of defects toward efficient perovskite solar cells, *Science Bulletin*, 2020, **65**, 2022-2032, doi: 10.1016/j.scib.2020.07.017.

[31] C. Shao, J. He, J. Ma, Y. Wang, G. Niu, P. Zhang, K. Yang, Y. Zhao, F. Wang, Y. Li, J. Wang, Multifunctional graphdiyne enables efficient perovskite solar cells *via* anti-solvent additive

engineering, *Nano-Micro Letters*, 2025, **17**, 121, doi: 10.1007/s40820-024-01630-y.

[32] L. Zhang, T. Chen, S. Zeng, H. Su, Effect of doping elements on oxygen vacancies and lattice oxygen in CeO_2 CuO catalysts, *Journal of Environmental Chemical Engineering*, 2016, **4**, 2785-2794, doi: 10.1016/j.jece.2016.05.023.

[33] Z. Huang, J. Song, X. Wang, L. Pan, K. Li, X. Zhang, L. Wang, J.-J. Zou, Switching charge transfer of $C_3N_4/W_{18}O_{49}$ from type-II to Z-scheme by interfacial band bending for highly efficient photocatalytic hydrogen evolution, *Nano Energy*, 2017, **40**, 308-316, doi: 10.1016/j.nanoen.2017.08.032.

[34] J. Li, Y. Wang, H. Song, Y. Guo, S. Hu, H. Zheng, S. Zhang, X. Li, Q. Gao, C. Li, Z. Zhu, Y. Wang, Photocatalytic hydrogen under visible light by nitrogen-doped rutile titania graphitic carbon nitride composites: an experimental and theoretical study, *Advanced Composites and Hybrid Materials*, 2023, **6**, 83, doi: 10.1007/s42114-023-00659-8.

[35] S. Wang, Y. Wang, X. He, Q. Lu, Degradation or humification: rethinking strategies to attenuate organic pollutants, *Trends in Biotechnology*, 2022, **40**, 1061-1072, doi: 10.1016/j.tibtech.2022.02.007.

[36] P. Amornpitoksuk, S. Suwanboon, Photocatalytic degradation of dyes by $AgBr/Ag_3PO_4$ and the ecotoxicities of their degraded products, *Chinese Journal of Catalysis*, 2016, **37**, 711-719, doi: 10.1016/S1872-2067(15)61078-6.

[37] J. Araña, J. M. Doña-Rodríguez, D. Portillo-Carrizo, C. Fernández-Rodríguez, J. Pérez-Peña, O. González Díaz, J. A. Navío, M. Macías, Photocatalytic degradation of phenolic compounds with new TiO_2 catalysts, *Applied Catalysis B: Environmental*, 2010, **100**, 346-354, doi: 10.1016/j.apcatb.2010.08.011.

[38] S. Deepracha, A. Ayral, M. Ogawa, Acceleration of the photocatalytic degradation of organics by *in situ* removal of the products of degradation, *Applied Catalysis B: Environmental*, 2021, **284**, 119705, doi: 10.1016/j.apcatb.2020.119705.

[39] Q. Zhao, M. Abdellah, Y. Cao, J. Meng, X. Zou, K. Enemark-Rasmussen, W. Lin, Y. Li, Y. Chen, H. Duan, Q. Pan, Y. Zhou, T. Pullerits, H. Xu, S. E. Canton, Y. Niu, K. Zheng, Size-dependent multi-electron donation in metal-complex quantum dots hybrid catalyst for photocatalytic carbon dioxide reduction, *Advanced Functional Materials*, 2024, **34**, 2315734, doi: 10.1002/adfm.202315734.

[40] P. Chang, Y. Wang, Y. Wang, Y. Zhu, Current trends on In_2O_3 based heterojunction photocatalytic systems in photocatalytic application, *Chemical Engineering Journal*, 2022, **450**, 137804, doi: 10.1016/j.cej.2022.137804.

[41] S. Wang, Q. Luo, W. Fang, R. Long, Interfacial engineering determines band alignment and steers charge separation and recombination at an inorganic perovskite quantum dot/WS_2 junction: a time domain *ab initio* study, *The Journal of Physical Chemistry Letters*, 2019, **10**, 1234-1241, doi: 10.1021/acs.jpclett.9b00285.

[42] Z. Tang, W. He, Y. Wang, Y. Wei, X. Yu, J. Xiong, X. Wang, X. Zhang, Z. Zhao, J. Liu, Ternary heterojunction in rGO-coated Ag/Cu_2O catalysts for boosting selective photocatalytic CO_2 reduction into CH_4, *Applied Catalysis B: Environmental*, 2022, **311**, 121371, doi: 10.1016/j.apcatb.2022.121371.

[43] C. Yin, L. Cui, T. Pu, X. Fang, H. Shi, S. Kang, X. Zhang, Facile fabrication of nano-sized hollow-CdS@g-C_3N_4 Core-shell spheres for efficient visible-light-driven hydrogen evolution, *Applied Surface Science*, 2018, **456**, 464-472, doi: 10.1016/j.apsusc.2018.06.137.

[44] J. Li, Y. Wang, X. Li, Q. Gao, S. Zhang, A facile synthesis of high-crystalline g-C_3N_4 nanosheets with closed self-assembly strategy for enhanced photocatalytic H_2 evolution, *Journal of Alloys and Compounds*, 2021, **881**, 160551, doi: 10.1016/j.jallcom.2021.160551.

[45] I. Papailias, N. Todorova, T. Giannakopoulou, N. Ioannidis, P. Dallas, D. Dimotikali, C. Trapalis, Novel torus shaped g-C_3N_4 photocatalysts, *Applied Catalysis B: Environment and Energy*, 2020, **268**, 118733, doi: 10.1016/j.apcatb.2020.118733.

[46] W. Zhang, Z. Zhang, S. Kwon, F. Zhang, B. Stephen, K. K. Kim, R. Jung, S. Kwon, K. B. Chung, W. Yang, Photocatalytic improvement of Mn-adsorbed g-C_3N_4, *Applied Catalysis B: Environmental*, 2017, **206**, 271-281, doi: 10.1016/j.apcatb.2017.01.034.

[47] H. Ding, D. Han, Y. Han, Y. Liang, X. Liu, Z. Li, S. Zhu, S. Wu, Visible light responsive CuS/protonated g-C_3N_4 heterostructure for rapid sterilization, *Journal of Hazardous Materials*, 2020, **393**, 122423, doi: 10.1016/j.jhazmat.2020.122423.

[48] A. Pan, X. Ma, S. Huang, Y. Wu, M. Jia, Y. Shi, Y. Liu, P. Wangyang, L. He, Y. Liu, $CsPbBr_3$ perovskite nanocrystal grown on MXene nanosheets for enhanced photoelectric detection and photocatalytic CO_2 reduction, *The Journal of Physical Chemistry Letters*, 2019, **10**, 6590-6597, doi: 10.1021/acs.jpclett.9b02605.

[49] S. He, R. Li, M. Xu, Y. Wang, R. Guo, N. Liu, Z. Mo, Water-stabilized perovskite $CsPbBr_3$/CsPb2Br5 for high-sensitivity fluorescence "on-off-on" recognition and cell imaging, *Chemical Engineering Journal*, 2025, **512**, 162689, doi: 10.1016/j.cej.2025.162689.

[50] S. Fang, Y. Xia, K. Lv, Q. Li, J. Sun, M. Li, Effect of carbon-dots modification on the structure and photocatalytic activity of g-C_3N_4, *Applied Catalysis B: Environmental*, 2016, **185**, 225-232, doi: 10.1016/j.apcatb.2015.12.025.

[51] X. Zhu, E. Zhou, X. Tai, H. Zong, J. Yi, Z. Yuan, X. Zhao, P. Huang, H. Xu, Z. Jiang, G-C_3N_4 S-scheme homojunction through van der waals interface regulation by intrinsic polymerization

tailoring for enhanced photocatalytic H_2 evolution and CO_2 reduction, *Angewandte Chemie International Edition*, 2025, **64**, e202425439, doi: 10.1002/anie.202425439.

[52] X. Qian, W. Li, X. Wang, H. Guan, Q. Bao, B. Zhao, B. Wulan, S. Liu, D. Zhu, X. Feng, J. Sun, Multifunctional roles of ionic microenvironments in the preparation, modification, and application of g-C_3N_4, *Advanced Functional Materials*, 2025, **35**, 2416946, doi: 10.1002/adfm.202416946.

[53] F. Ni, M. Xie, T. Liu, X. Zhou, Z. Chen, K. Zheng, Y. Wu, Q. Zhao, C. Yang, Aggregation-induced delayed fluorescence for time-resolved luminescence sensing of carboxylesterase in living cells, *Chemical Engineering Journal*, 2022, **437**, 135396, doi: 10.1016/j.cej.2022.135396.

[54] X. Xu, Y. Pan, Y. Zhong, R. Ran, Z. Shao, Ruddlesden–popper perovskites in electrocatalysis, *Materials Horizons*, 2020, **7**, 2519-2565, doi: 10.1039/d0mh00477d.

[55] S. Fang, M. Rahaman, J. Bharti, E. Reisner, M. Robert, G. A. Ozin, Y. H. Hu, Photocatalytic CO_2 reduction, *Nature Reviews Methods Primers*, 2023, **3**, 61, doi: 10.1038/s43586-023-00243-w.

[56] J. Kaur, S. C. Peter, Two-dimensional perovskites for photocatalytic CO_2 reduction, *Angewandte Chemie International Edition*, 2025, **64**, e202418708, doi: 10.1002/anie.202418708.

[57] R. Bhimpuria, M. Tomar, A. Thapper, M. Ahlquist, K. E. Borbas, Photocatalytic product-selective reduction of CO_2, CO, and carbonates, *Chem*, 2025, **11**, 102450, doi: 10.1016/j.chempr.2025.102450.

[58] Q. Chen, X. Lan, Y. Ma, P. Lu, Z. Yuan, J. Shi, Boosting $CsPbBr_3$-driven superior and long-term photocatalytic CO_2 reduction under pure water medium: synergy effects of multifunctional melamine foam and graphitic carbon nitride (g-C_3N_4), *Solar RRL*, 2021, **5**, 2100186, doi: 10.1002/solr.202100186.

[59] Z. Asghar, M. W. S. Khan, A. Alhashash, M. A. Gondal, Biomechanical analysis of cilia-induced liquid propulsion in rough porous passageway under magnetic field control: MATLAB- and Mathematica-based simulations, *Chinese Journal of Physics*, 2025, **95**, 455-475, doi: 10.1016/j.cjph.2025.02.028.

[60] Z. Asghar, M. W. S. Khan, M. A. Gondal, A. Ghaffari, Magnetohydrodynamic flow of Carreau Yasuda fluid inside a complex wavy passage formed by beating cilia: a finite-difference analysis, *Proceedings of the Institution of Mechanical Engineers, Part E: Journal of Process Mechanical Engineering*, 2025, **239**, 87-98, doi: 10.1177/09544089231171037.

[61] M. Ashfaq, Z. Asghar, Y. Nie, M. A. Gondal, Heat transfer analysis in MHD curved channel flow with ciliated walls: Numerical solutions with error control, *Thermal Science and Engineering Progress*, 2025, **64**, 103765, doi: 10.1016/j.tsep.2025.103765.

[62] Z. Asghar, M. W. S. Khan, W. Shatanawi, M. A. Gondal, A. Ghaffari, An IFDM analysis of low Reynolds number flow generated in a complex wavy curved passage formed by artificial beating cilia, *International Journal of Modern Physics B*, 2023, **37**, 2350187, doi: 10.1142/s0217979223501874.

[63] Z. Asghar, M. W. S. Khan, N. Ali, M. Waqas, On IFDM simulation of Oldroyd 8-constant fluid flowing due to motile microorganisms, *Chinese Journal of Physics*, 2025, **93**, 158-171, doi: 10.1016/j.cjph.2024.11.033.

[64] M. W. S. Khan, Z. Asghar, W. Shatanawi, M. A. Gondal, Surface roughness analysis of cilia-driven flow for shear-thinning fluid inside a horizontal passage, *Physics of Fluids*, 2024, **36**, 103108, doi: 10.1063/5.0227610.

[65] Z. Asghar, K. U. Rehman, W. Shatanawi, M. W. S. Khan, Efficiency optimization of micro-swimmers in viscoelastic bio-fluids within complex cervical environments, *Chinese Journal of Physics*, 2025, **96**, 664-677, doi: 10.1016/j.cjph.2025.06.003.

[66] L. Fang, Y. Guo, S. Zhang, Y. Lv, Y. Xue, X. Bai, J. Li, C. Lai, Y. Wang, Influence of transition metal substitution on $Cs_2AgBiBr6/M_3C_2$ (M = Ti, V, Cr, Zr, Nb, Mo, Hf, Ta, and W) interfaces: First-principles and experimental studies, *Applied Surface Science*, 2023, **641**, 158538, doi: 10.1016/j.apsusc.2023.158538.

[67] Y. Guo, S. Zhang, Z. Zhang, Y. Xue, J. Li, H. Song, Y. Wang, Q. Shen, Adhesion, stability, structural and electronic properties of perovskite/$BaWO_4$ heterostructures: first-principles and experimental characterizations, *Inorganic Chemistry Frontiers*, 2024, **11**, 2661-2671, doi: 10.1039/D4QI00231H.

[68] H. Li, Q. Wang, Y. Oteki, C. Ding, D. Liu, Y. Guo, Y. Li, Y. Wei, D. Wang, Y. Yang, T. Masuda, M. Chen, Z. Zhang, T. Sogabe, S. Hayase, Y. Okada, S. Iikubo, Q. Shen, Enhanced hot-phonon bottleneck effect on slowing hot carrier cooling in metal halide perovskite quantum dots with alloyed A-site, *Advanced Materials*, 2023, **35**, e2301834, doi: 10.1002/adma.202301834.

Publisher's Note: Engineered Science Publisher remains neutral with regard to jurisdictional claims in published maps and institutional affiliations.

Open Access